Acta Materialia 149 (2018) 19–28

Contents lists available at ScienceDirect

Acta Materialia

journal homepage: www.elsevier.com/locate/actamat

Full length article

Dislocation-based modeling of long-term creep behaviors of Grade 91 steels

Jifeng Zhao [a, *], Jiadong Gong [a], Abhinav Saboo [a], David C. Dunand [b], Gregory B. Olson [a, b]

[a] QuesTek Innovations LLC, 1820 Ridge Avenue, Evanston, IL 60201, USA
[b] Northwestern University, Dept. of Materials Science & Engineering, 2220 Campus Drive, Evanston, IL 60208, USA

ARTICLE INFO

Article history:
Received 29 September 2017
Received in revised form
27 January 2018
Accepted 1 February 2018
Available online 8 February 2018

Keywords:
Grade 91 ferritic steel
Creep modeling
Dislocation climb
Dislocation detachment
Creep threshold stress
Z phase
Precipitation strengthening mechanism

ABSTRACT

To meet the 30 years (~263,000 h) design lifetime of a typical thermal power plant, understanding and modeling of the long-term creep behaviors of the power plant structural steels are critical to prevent premature structural failure due to creep. The extremely long exposure to high operation temperature results in evolving microstructure during service, which cannot be observed in standard short-term (<1 year) creep tests. In fact, creep rupture life predictions based on short-term creep testing data often overestimate the creep rupture times for long period of time, and are therefore insufficient to provide a reliable failure time prediction. In this article, a microstructure-sensitive, long-term creep model is developed and validated against existing long-term creep experimental data (~80,000 h) for ferritic steel Grade 91 (Fe-8.7Cr-0.9Mo-0.22V-0.072Vb-0.28Ni in wt.%). The mechanistic creep model is based on fundamental dislocation creep mechanisms – the particle bypass model based on dislocation climb from Arzt and Rösler [1] - that describe the steady state creep strain rate as a function of stress, temperature, and microstructure. In particular, the model incorporates the evolution of the particle size via coarsening into the dislocation climb theory, dislocation detachment mechanism and back-stress generated by subgrain dislocation structures. Model inputs were obtained based on the microstructure information obtained from published literature from the National Institute of Material Science (NIMS, Japan) creep database. The model, which can be used on many types of alloys, shows excellent agreement with existing long-term creep experimental data (~80,000 h) of Grade 91 ferritic steel.

1. Introduction

The lifetime of a power plant can be in excess of 30 years (~263,000 h), which requires outstanding creep resistance of load-bearing structural steels to prevent the premature power plant component failure. Grade 91 steels have been used as one of the major structural steels for Advanced Ultra Supercritical (AUSC) [2] power plants due to its outstanding high-temperature creep resistance [2], [3]. Components made of the Grade 91 ferritic steel (with 9 wt% Cr and 1 wt% Mo as major alloying elements, micro-additions of V and Nb, 0.1 wt% C and a controlled nitrogen content [4]) are experiencing a wide array of internal stresses depending on the location and welds [5]. Typical supercritical fossil fueled power stations operate at a steam pressure typically above 24 MPa (3.5 ksi) with steam temperatures of 538–566 °C (1000–1050 F) or higher [6]. In the hottest part of the boiler and for components such as headers, tubes, and pipes, the hoop stress can be as high as 100 MPa [5]. Creep test data under these conditions are essential to ensure a reliable power plant design that exceeds 30 years in lifetime. However, laboratory-scale creep test data of Grade 91 steels are not available up to 300,000 h. Fig. 1 shows one of the longest existing laboratory test data for creep rupture time as a function of the applied stresses and temperature for both 9%Cr (Grade 91) and 12%Cr (T122) steel, which are approaching 100,000 h creep rupture time (11.5 years). A "secondary-like" minimum creep rate, stable at $2 \pm 1 \times 10^{-7}$ h^{-1}, is maintained over a very long time span of 40,000 h. During this 4.5 year duration, the microstructure is evolving extremely slowly. Therefore, we assume a quasi steady-state condition (dislocation motion, diffusion process) in the model derivation for this "secondary-like" creep. Nevertheless, when plotting creep rupture time vs. stress (Fig. 1(a)), accelerated reduction of creep rupture time occurs in the long-term creep region (>40,000 h), which has to be separated from the short-term region and is represented by a steeper slope in a creep rupture

* Corresponding author.
E-mail address: zhaojf06@gmail.com (J. Zhao).

https://doi.org/10.1016/j.actamat.2018.02.001
1359-6454/

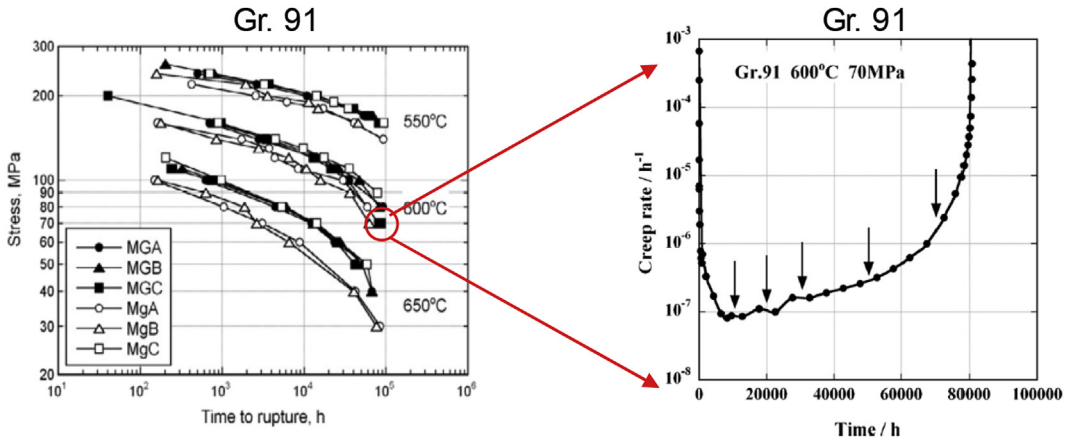

Fig. 1. (a) Double logarithmic plot of applied stress vs. time to rupture for ferritic steels with 9% Cr (Grade 91) (b) Semi-logarithmic plot of creep rate vs. time for steel Grade 91 at 600 °C and 70 MPa, showing primary, secondary-like (~1–3 x 10^{-7} h^{-1}) and tertiary creep regions (beyond ~40,000 h). Arrows indicate the times at which creep tests were interrupted to obtain the microstructure information by the replica technique (see Fig. 2). [22], [25] [26] [39].

time vs. stress regression plot such as Fig. 1(a). Consequently, simple extrapolation from short-term creep rupture time overestimate the long-term creep rupture time, which necessitate more complex models [[7–10]] and motivates the development of a microstructure-based creep model capable of predicting premature creep failure for the long-term creep regime.

The low applied stress region (long-term creep) is characterized by high creep exponent in the classical power law relationship. For single-phase metals and alloys, minimum (secondary) strain rates $\dot{\varepsilon}$ can be written as a power law of the applied stress σ:

$$\dot{\varepsilon} = A\frac{DGb}{k_B T}\left(\frac{\sigma}{G}\right)^{n_{app}} \quad (1)$$

where A is a constant, D is the vacancy diffusion coefficient, G the shear modulus, b the Burgers vector, and n is the stress exponent which is predicted to be 3–5 based on the classical dislocation climb and glide mechanisms. We use here the conventional approaches of secondary, minimum creep rate in Eq (1) as an approximation for the near-constant "secondary-like" minimum creep rates, which are stable over periods of years (Fig. 1(a)) but nevertheless associated with very slow microstructure evolution.

However precipitation-strengthened alloys usually exhibit a very high stress exponent, labelled the apparent stress exponent n_{app} when using Eq. (1), which is stress- and temperature-dependent [11], [12]. According to NIMS published creep tests database, when the applied stress is in the range of 70–130 MPa, Grade 91 has an apparent stress exponent n_{app} ranging from 6 to 12 at 600 °C. This high stress sensitivities can be explained by introducing a threshold stress σ_{th}.

$$\dot{\varepsilon} = A\frac{DGb}{k_B T}\left(\frac{\sigma-\sigma_{th}}{G}\right)^{n} \quad (2)$$

where n is the stress exponent of the matrix, which leads to arbitrarily high apparent stress exponent n_{app} on the plot of $\log(\dot{\varepsilon}) - \log(\sigma)$ near σ_{th}. Electron microscopy observations and theories suggest that the threshold stress for precipitation-strengthened alloys is due to the interactions between the matrix dislocations and the particles during climb bypass [13]. Many theories have been proposed to explain to the origin of the threshold stress due to unshearable precipitates or dispersoids, including local and general climb theory, dislocation detachment theory, and back-stress induced by subgrain structures. For incoherent dispersion-strengthened alloys, Arzt and Rösler [14] predicted a threshold stress using a local climb theory, where new dislocation line is created as the dislocation climbs around the matrix-precipitate interface during the bypass process. However, the local climb is an unstable process where the sharp bend of dislocation can be rapidly relaxed by vacancy diffusion leading to a more "general" climb process [14], [15]. Arzt and Rösler [14] calculated the detailed dislocation profiles based on the condition of minimum energy, which leads to the combination of local and general climb as the stable dislocation configurations. These authors [1] later suggested that a threshold stress can furthermore arise from an attractive interaction between the dislocation and incoherent dispersoid at the detachment side [16], which occurs after the dislocation has surmounted the obstacles by climb. In addition, Dunand and coworkers proposed that the threshold stress due to climb is affected by the lattice strain induced by the lattice parameter and the stiffness mismatches between matrix and coherent precipitates, which changes the net forces on the climbing dislocation [17], [18]. Subgrains are dislocation networks with low misorientation (1° or 2° angle) boundaries [19] [20], in martensitic hierarchical structures whereas prior austenite grain boundaries and martensitic block boundaries are high-angle grain boundaries. The coarsening of subgrain structures are observed to be detrimental to the creep failure [21], [22]. It is supported by experimental observations that subgrain structures create long-range internal stresses that locally reduces the effective applied stress for both monotonic and cyclic loading [23], [24]. This effect can be leveraged by the introduction of threshold stress in Eq. (2).

These experimental observations and theories elucidate the interaction between dislocation and the nano-sized particles from which a steady state creep rate can be then calculated. Here, we follow Arzt and Rösler's approaches and derive a mathematical expression of creep strain rate based on the fundamental physics of dislocation climb mechanisms (around MX particles) for Grade 91 steels. Back stress contributed from the evolving subgrain dislocation structures is also accounted for in the model framework, as is the evolving precipitation sizes and volume fractions during creep deformation. These two microstructure-sensitive mechanisms both have been considered in a unified modeling framework. Necessary microstructure information are obtained from interrupted creep tests performed by NIMS [25]– [27] as the model inputs. Model predictions of the steady-state strain rate of Grade 91 show excellent agreement with experiments.

2. Modeling approach

2.1. Microstructure evolution

The composition of the commercial Grade 91 steel is shown in Table 1. As processed Grade 91 steel has, before creep exposure, a tempered martensitic hierarchical microstructure. As illustrated by the schematics in Fig. 2(b), prior austenite grain boundaries (PAGB) are divided into martensitic packets, which are aggregates of martensitic blocks on the same plane [28]. Therefore packets can be divided into martensitic blocks, which further contain subgrain dislocation structures/lath structures. As both martensitic blocks and packets are bound by high-angle boundaries, they are generally referred to as "grains". Subgrain-scale dislocation structures are bounded by low-angle boundaries [19], [29]. Excessive coarsening of subgrains has been observed during long term creep tests in Fig. 7 that contributes to the loss of creep resistance and dictates the final creep failure. Two types of precipitates are initially present. First, $M_{23}C_6$ carbides with ~0.1 μm size [26], which are nucleated predominantly at the prior austenite grain boundaries, and along martensite lath boundaries after tempering. Oruganti [30] suggests that the existence of $M_{23}C_6$ particles effectively pin the subgrain boundaries, therefore providing creep resistance. Second, nano-sized MX carbonitride precipitates, which are finely distributed inside the matrix, provide significant resistance against dislocation motion. Both $M_{23}C_6$ and MX particles thus control long-term creep deformation.

In conventional creep theories, the microstructure is usually assumed to be stable through the steady state creep period, which results in a constant strain rate in the secondary creep stage. However the National Institute for Materials Science (NIMS, Japan) performed interrupted creep tests on steel Grade 91 and illustrated a very slowly evolving microstructure due to thermal exposure during the very long testing times used, as shown in Fig. 2 [5]. Microstructures are examined by both transmission electron microscopy (TEM) and scanning TEM in conjunction with energy-dispersive X-ray analysis (STEM-EDX) at 200 kV. Thin foils for TEM study are prepared at the gauge section of crept samples after creep test interruption. STEM-EDX is performed to determine the composition of each precipitations. Micrographs in Fig. 2 (a)-(f) are taken at the times corresponding to the arrows in Fig. 1 (b). These observations elucidate that the microstructure is evolving during the long creep experiments, spanning 10,000 to 81,000 h (1.1–9.2 years). First, the MX carbo-nitride precipitates which interact with dislocations are dissolving, thus reducing creep resistance. Second, the $M_{23}C_6$ precipitates at (sub)grain boundaries are coarsening, thus significantly decreasing the pinning forces for subgrain boundary migration and also decreasing to the creep resistance. Third, at a later stage during creep, Z-phase particles are formed and coarsen rapidly at the expense of the beneficial MX carbonitride, which leads to reduced creep resistance and accelerated creep strain rate after long-term thermal exposure. Up to 10,000 h, the number density and radius of the MX precipitates are relatively stable in the short-term creep regime. Only after long-term creep do the MX nitrides, with composition (V,Nb)N, transform into Z-phase nitride Cr(V,Nb)N by Cr diffusion into the precipitates. Therefore, the microstructure evolution is key to modeling the long-term creep behavior of the Grade 91 steel; it is the primary goal of this work to achieve integrate microstructural evolution model for dissolution, coarsening and growth of precipitates into models that consider interaction of dislocations with these precipitates to predict macroscopic strain rates.

Table 1
Composition (wt.%) of commercial Grade 91 steel [25].

	C	Si	Nb	V	N	Ni	Cr	Mo	Cu
Grade 91	0.09	0.29	0.072	0.22	0.044	0.28	8.7	0.90	0.032

2.2. Creep modeling (Arzt and Rösler theory)

Due to the very slow evolution of the microstructures occurring over a timescale of years, it is reasonable to assume a local steady-state condition in the "secondary-like" creep stage. The creep model developed in this article follows the earlier approach by Arzt and Rösler [1], [14]. Consider particles (MX) dispersed at a low volume fraction within a matrix. At high temperature, if shearing is not operational, such obstacles are bypassed by matrix dislocations via a climb mechanism [14]. The particles are assumed to have a simplified geometry with a rectangular cross section (Fig. 3). The shear stress necessary for particle by-pass by athermal dislocation bowing, given by the Orowan stress, is an upper bound. When the shear stress acting on the dislocation is below the Orowan stress, the dislocation glides until it become pinned by the particles. As depicted in Fig. 3, the dislocation climbs up on the particle to position z_0 aided by vacancy diffusions. The climbing face is inclined at an angle β to the glide plane of the dislocation. Under the action of its line tension, a distance x_0 of the dislocation line is unraveled out of the glide plane.

According to the Orowan-Taylor equation, the steady state creep rate $\dot{\varepsilon}$ can be written as a function of the average dislocation velocity v as:

$$\dot{\varepsilon} = \rho b v = \rho b \frac{\lambda}{t_c + t_g} \approx \rho b \frac{\lambda}{t_c} \tag{3}$$

where b is the burger's vector, ρ is the mobile dislocation density, λ is the particle spacing, t_c is the time that dislocation climbs over a particle, t_g is the time dislocation glides to the next particle. Assuming that the dislocation climb is the rate-controlling process, (i.e., the dislocation climb time $t_c \gg t_g$), then the dislocation velocity can then be simplified as $v = \lambda / t_c$. Based on Artz and Rösler's work, dislocation climb time is contributed by dislocation general climb, local climb and/or detachment mechanisms:

$$t_c = t_{general} + t_{local} + t_{detachment} \tag{4}$$

2.2.1. Dislocation climb mechanism

Fig. 4 depicts the projection of dislocation lines on the x-z plane, where one or both related climbing modes co-exist, i.e., local climb and general climb. Local climb indicates that, when the dislocation is climbing over the particles, the dislocation line is confined closely to the particle interface with sharp bending corners, which is a preferred configuration at high applied stress (Fig. 4(a)). By contrast, general climb occurs at lower applied stresses with a lower strain rate, which allows for vacancy diffusion to relax the dislocation profile to leave the particle interface and form a smooth curve (Fig. 4(b)). Arzt and Rösler [14] calculated the equilibrium dislocation line profile subject to a condition of minimum energy. This work elucidates that the stress required for stable local climb is as high as Orowan looping stress. At an intermediate applied stress below the Orowan stress, the local climb is an energetically unstable process and therefore a "strictly" local climb process does not occur.

Instead, the two climb modes co-exist during the dislocation climbing process as shown in Fig. 4 (c). Arzt and Rösler's work is based on the assumption that line energy T of the dislocation

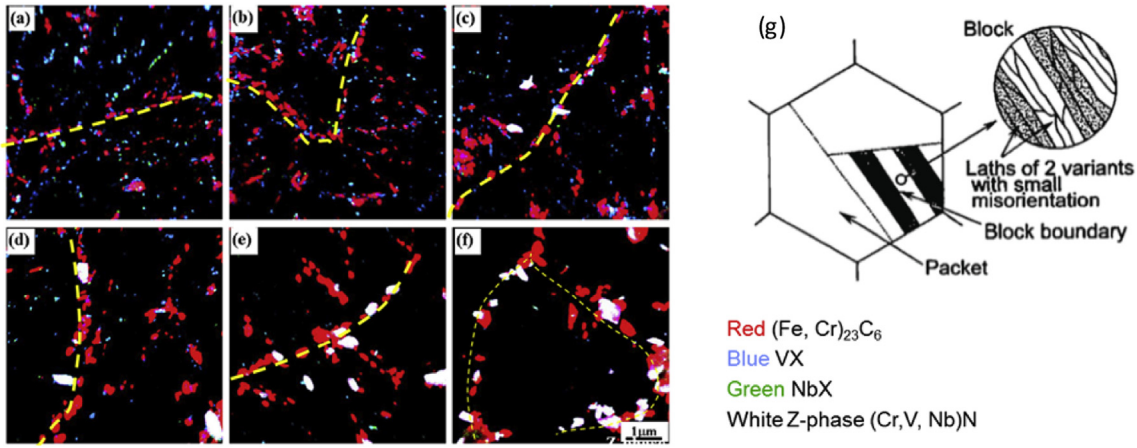

Fig. 2. Micrograph showing microstructure evolution of Grade 91 steels during creep test at 600 °C; under 70 MPa at (a) as tempered (b) 10,000 h (c) 30,000 h (d) 50,000 h (e) 70,000 h (f) 81,000 h (Figure (a)–(f) are taken from Ref. [5]). Evolution of the four types of precipitates are represented by different color codes. Red particles indicate the $M_{23}C_6$ particles, blue represents the VX carbonitride, green represents the NbX carbonitride, Z phase is represented by white color. The yellow dotted line indicates the prior austenite grain boundaries. (g) Schematic of the hierarchical microstructure that consists of prior austenite grain boundary, martensitic blocks and subgrain dislocation structures [29]. (For interpretation of the references to color in this figure legend, the reader is referred to the Web version of this article.)

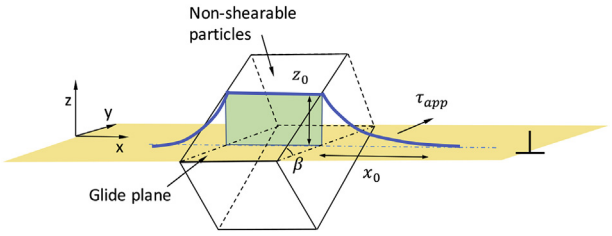

Fig. 3. Schematics of dislocation climb over non-shearable particles after [17] [1], [14].

segment residing in or near the particle-matrix interface $L_{interface}$ is reduced by a factor of k compared to the line energy of a dislocation segment remote from the particle as L_{remote}:

$$L_{interface} = kL_{remote} \tag{5}$$

The line energy reduction makes the particle-matrix interface an energetically favorable place for the dislocation movement, which (i) stabilizes the local climb mode on a portion of dislocation segment and (ii) also introduces an attractive interaction between dislocation and particle on the departure side. At an intermediate applied stress, the dislocation starts interacting with particles via the general climb. The equilibrium profile of the dislocation line was calculated based on the energy minimum:

$$\frac{d}{x_0} = \sqrt{1-\left(\frac{\tau_{eff}}{\tau_O}\right)^2} \cdot \left(\frac{x_0}{z_0}+\frac{z_0}{x_0}\right) \cdot \left[\frac{\tau_{eff}}{\tau_O}\frac{1}{tan\beta} - 1 + \left(1-\frac{z_0}{x_0}\right)^{9/4}\right] \tag{6}$$

where x_0, z_0 and β are defined in Fig. 4 (a) and (c), which describes the dislocation equilibrium profile, τ_O is the Orowan stress, τ_{eff} is the local effective applied stress (modified by a back stress as in Eq. (15) due to the subgrain dislocation structures, as discussed in the next section). The solution of x_0 at a given z_0 cannot be explicitly written, since x_0 and z_0 are implicitly coupled together. Instead, Eq. (6) can be solved numerically by using Brent's root finding method. As the dislocation climbs over a particle, both x_0 and z_0 are increasing until a critical position (x_0^*, z_0^*) is reached. After this critical point, the local climb mode is switched on for a portion of the dislocation line segment as shown in Fig. 4 (c), which becomes the energetically favorable climb mode. The critical position (x_0^*, z_0^*) can be calculated as [1]:

$$\frac{z_0^*}{x_0^*} = \frac{1-\sqrt{1-\left(\frac{k}{cos\beta}\right)^2+\left(\frac{\tau_{eff}}{\tau_O}\right)^2 tan^2\beta}}{\frac{k}{cos\beta}+\frac{\tau_{eff}}{\tau_O}tan\beta} \tag{7}$$

The solutions for the dislocation profiles are illustrated in Fig. 5 for four different applied stresses. At lower applied stress, general climb occurs throughout the climbing history. As the applied stress

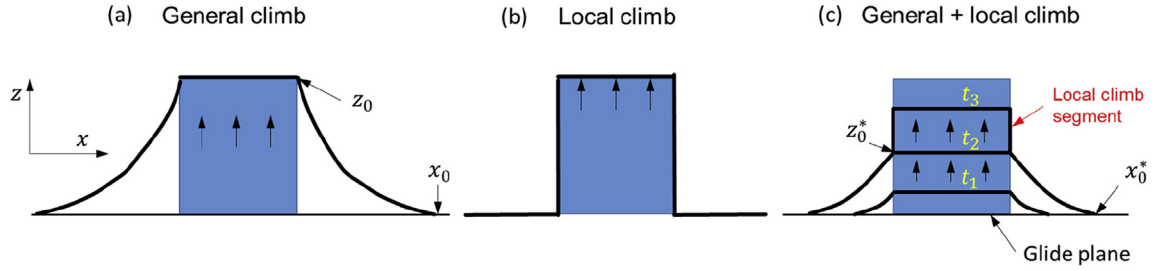

Fig. 4. Schematic of dislocation climb mechanism (a) general climb (b) local climb (c) general + local configuration for various times t_1, t_2, t_3.

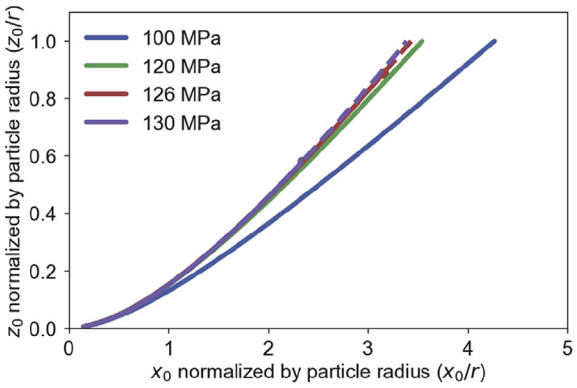

Fig. 5. Equilibrium dislocation profile z_0 and x_0 at 600 °C with $k = 0.85$. Solid line and dashed line indicate the general and local climb respectively. The stresses displayed in the legend are the total applied stress τ_{app} instead of τ_{eff}.

increases, the dislocation line tends to bend over to a greater degree, resulting in a smaller x_0 at a given z_0. As the applied stress further increases, the local climb mode is achieved. The higher the local stress is, the earlier this local climb mode is turned on, which is consistent with the physical understanding that local climb is preferred as a higher stress.

Following Arzt and Rösler [14], the climb rate is written as a function of the chemical potential of the dislocation line μ:

$$\frac{dy}{dt}(x_0,\ z_0) = C_i \frac{|\mu(x_0,\ z_0,\ \lambda,\ \tau)|}{|dA_{ABD}/dy(x_0,\ z_0)|} \tag{8}$$

where A_{ABD} is the area under the climbing segment A-D projected in the direction Burger's vector and C_i is a kinetic constant proportional to the volume diffusivity D_v:

$$C_i = \frac{2\pi D_v d}{k_B T b} \tag{9}$$

where d is the particle diameter ($d = 2r$). The chemical potential μ can be written as a function of particles spacing λ, applied stress τ, and the climb mode. More detailed discussions of Eqs. (6)–(8) can be found in Refs. [1], [14]. The MX particle spacing can be calculated as a function of the particle radius r and volume fraction f:

$$\lambda = r\left(1.23\sqrt{\frac{\pi(1-1/3\eta)}{f}} - 2\right) \tag{10}$$

where η is the particle aspect ratio taken here as unity, as the MX particles are assumed to be spherical Finally, the time needed for the dislocation to climb and bypass the particle can be calculated by integrating the climb rate over the climbing height:

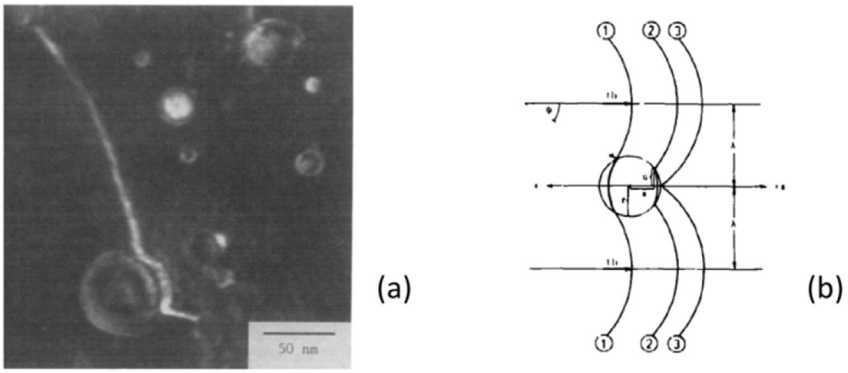

Fig. 6. Dislocation detachment mechanisms, reprinted from Ref. [31] (a) TEM images of dislocation are attracted at the particle interface for dispersion-strengthened superalloy MA 6000 and (b) schematics of dislocation detachment mechanism.

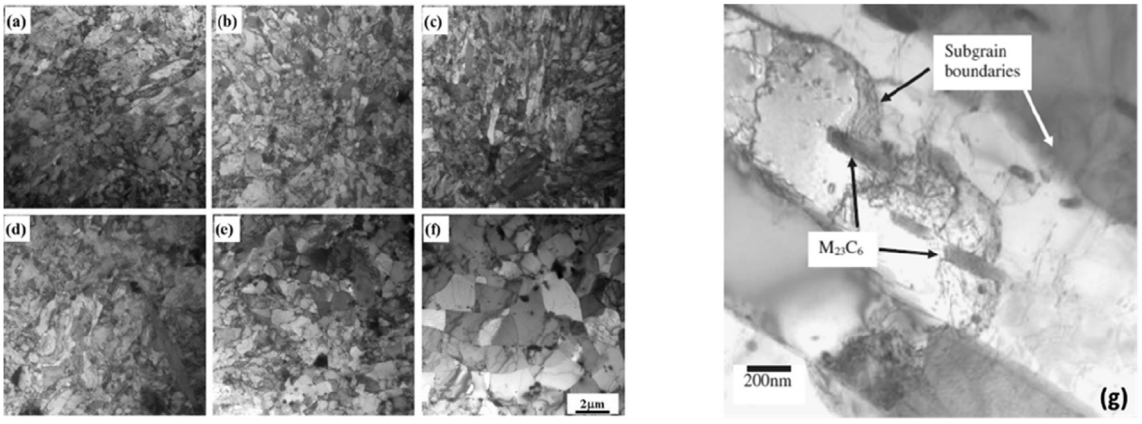

Fig. 7. (a–f) Dislocation substructure evolution during the same creep tests as in Fig. 2 obtained from Sawada [25]. (g) Subgrain boundary bowing between $M_{23}C_6$ particles under the influence of stress (from Oruganti [38]).

$$t_c = \int_0^{y^*} \frac{1}{(dy/dt)_{gen}} dt + \int_{y^*}^{r} \frac{1}{(dy/dt)_{local}} dt \tag{11}$$

Introducing Eq. (11) into the Orowan relation in Eq. (3), the steady-strain rate can then be calculated.

2.2.2. Dislocation detachment mechanism

As discussed further by Arzt and Rösler [1], a direct consequence of the line energy reduction in Eq. (5) is that it leads to an attractive particle-dislocation interaction, which results in a threshold stress behavior associated with the detachment process after the climb bypass has been completed. The dislocation detachment mechanism has been widely accepted in the literature. Fig. 6 shows an example of a dislocation at the departure side of an oxide disperoid in a nickel matrix, where the dislocation line is clearly pinned at the departure side of the particle-matrix interface as expected if an attractive particle-dislocation interaction is present. A threshold stress is then required for the dislocation to complete the detachment process, below which the dislocation is trapped at the particle and creep strain rate is thus negligible. The threshold stress $\tau_d(T)$ is calculated as a fraction of the Orowan stress τ_o in shear by Arzt and Rösler [1] as:

$$\frac{\tau_d(T)}{\tau_o} = \sqrt{1 - \left(k + \frac{2k_BT}{Gb^2d} ln\left(\frac{\dot{\varepsilon}_0}{\dot{\varepsilon}}\right)\right)^2} \tag{12}$$

Where T is the temperature, $\dot{\varepsilon}$ is the strain rate, $\dot{\varepsilon}_0$ is the reference strain rate (e.g., that of the particle-free material at the same stress). The value $\dot{\varepsilon}_0/\dot{\varepsilon} = 10^{10}$ [31] is adopted in this work. It is noted that the detachment process is considered to be a thermally-activated event, where the athermal threshold limit is found to be $\tau_d = \tau_o\sqrt{1-k^2}$ at $T = 0K$. At a finite temperature, thermal activation assists the detachment process from the particle, even if the stress is below the athermal threshold limit.

When $\tau_{eff} > \tau_d(T)$, detachment barriers are overcome instantly therefore time for detachment to complete $t_{detach} = 0$. When $\tau_{eff} < \tau_d(T)$, the detachment process is considered as a thermally-activated event, whose kinetic can be described as:

$$\tau_{eff} < \tau_d(T)\ t_{detach} = 1 \Big/ \frac{3D_v}{b^2} exp\left(-\frac{Gb^2r\left[(1-k)\left(1-\frac{\tau_{eff}}{\tau_d(T)}\right)\right]^{3/2}}{k_BT}\right) \tag{13}$$

$$\tau_{eff} > \tau_d(T),\ t_{detach} = 0 \tag{14}$$

Finally introducing Eq. (13) (14) and (11) into Eq. (4) and. (3) leads to a mathematical representation of the steady-state creep strain rate. Shear stresses are utilized in the derivation which can be converted to tensile stresses can by $\sigma = M\tau$, where $M = 3$ is the appropriate Taylor factor (or reciprocal of the Schmid factor for single crystals).

2.2.3. Back stress model/subgrain dislocation structures

Evolution of subgrains under creep loading is observed in Grade 91 ferritic steels, which also contributes to the high temperature creep resistance [32–34]. In a typical martensitic hierarchical microstructure, subgrains are dislocation networks with low misorientation (1° or 2° angle) boundaries [19] [20], whereas prior austenite grain boundaries, packet and block boundaries are high-angle grain boundaries. The subgrain structure will migrate (coarsen) during creep deformation as shown in Fig. 7, which contributes to strain and is thus detrimental to the creep life. It has been shown that the creep strain acceleration is well correlated with the subgrain dislocation coarsening based on NIMS creep tests and Rustam [28]. Bazazi [35] showed that the coarsening of the subgrains has a strong influence on the decrease of material hardness under creep conditions. Moreover, these subgrain boundaries are pinned by the $M_{23}C_6$ carbides and Nb-rich M(C, N) carbonitride that are precipitated on these boundaries. Therefore the dissolution of MX particles and coarsening behaviors of pinning $M_{23}C_6$ carbides have a strong influence of these subgrain boundaries coarsening and must be modeled.

It has been widely accepted that the subgrain boundaries networks (cells) create a long-range internal stress, i.e., a back stress, for both cyclic and monotonic loading. The back stress τ_{back} is interpreted as an internal material resistance due to subgrain dislocation networks and it locally reduces the applied stress $\tau_{applied}$ (resolved on the glide plane from the applied tensile stress):

$$\tau_{eff} = \tau_{applied} - \tau_{back} \tag{15}$$

The presence of significant levels of dynamic internal stresses due to subgrain structures has been observed by Takeuchi [36] and Argon [33] experimentally. Although a large of body of literature has been dedicated to studying the subgrain dislocation structure, the exact mechanism that causes these significant internal stresses is still not completely understood and under active research. Mughrabi [23] [37], advocated that the internal stress arises due to different yield stresses of subgrain walls (hard) and interior regions (soft). Since the hard and soft regions yield at different stresses, the "composite" therefore has a heterogeneous stress state upon loading, which leads to a non-zero internal stress even after the applied stress is removed and successfully explained the Bauschinger effect in fatigue. However, this theory is less applicable in creep since macroscale material yielding is unlikely to occur during creep under very low applied stress.

Here, we adopt a theory which we believe to be more suitable for modeling creep deformation, as originally suggested by Argon [33] and further modified by Oruganti [30] for ferritic steel. In creep deformation, the migration of subgrain boundaries is impeded by pinning particles. Fig. 7 (g) shows a subgrain boundary in the process of breaking away from a set of $M_{23}C_6$ particles. The boundary is bowed between the particles, and dislocation debris is observed around the particles from which the boundaries have broken away. As a result, the bowing process generates significant long-term stress field. As suggested by Oruganti [30] [38], the back stress can be written as:

$$\tau_{back} = 0.26(1-\nu)\frac{\delta^{4/3}\theta^{1/3}}{b^{1/3}S}\sigma_{app} + \frac{K''}{\sqrt{B}} \tag{16}$$

where δ is the inter-carbide ($M_{23}C_6$) spacing on the subgrain boundaries, θ is the average misorientation angle (in radians) between adjacent subgrains, b is the Burger's vector, S is the average width of the subgrains, ν is the Poisson's ratio, B is the high-angle martensitic block size, and K'' is a coefficient. The first terms on the right-hand side of Eq. (16) denotes the contribution from subgrain structure, which is inversely proportional to the subgrain size S and scales with the external applied stress linearly. The second term is generated by high-angle grain boundary (blocks), similar to a Hall-Petch type relationship. These stresses are generated at the block boundaries through geometrically necessary dislocations (GND) that accommodate strain compatibility between adjacent blocks. It is noted that the block boundary migration is negligible during creep, therefore $K''/\sqrt{B}$ is taken as a constant value currently in this work.

3. Modeling results

The two microstructure-sensitive models (pinning of dislocations by finer MX particles, Section 2.1 and 2.2, and back-stress from subgrain boundaries pinned by larger $M_{23}C_6$ carbides, Section 2.2.3) are connected via Eq. (14). These two models have never been, to our knowledge, connected, as they pertain to two different particle sizes. The presence of both types of particles in Grade 91 steel however dictates the use of a combined modeling approach. The microstructural parameters used in the combined model are listed in Table 2. The microstructural parameters (r, λ) at 10,000, 30,000, 50,000 and 70,000 h during creep were characterized in interrupted creep tests at NIMS [25] [26] [39], and taken as inputs to the creep model. The MX particle radius remains relatively constant, but the MX area number density is reducing rapidly as a result of precipitation of Z phase (in white in Fig. 7). By varying the number density and radius of MX particles as the inputs, the creep model is capable of predicting the evolution of steady state strain rate during the creep test (see Table 3). The model prediction and experimental data of strain rate history agree well, as shown in Fig. 8 at 600 °C for a 70 MPa applied tensile stress. Model parameter sensitivity study is performed in Fig. 9.

The good agreement between experiments and model predictions in Fig. 8 is a strong indication that (i) microstructure fundamentally determines the steady state creep behaviors in long-term tests, (ii) MX particles and dislocation interaction - including detachment, local and general dislocation climb - control creep resistance for Grade 91 steel in the steady-state creep stage, (iii) Z phase nucleation and growth effectively reduces the beneficial MX particle number density and accelerates the creep strain rate during deformation, which potentially causes premature creep failures. It is noted that the model prediction departures from the experimental results at the longest creep time around 70,000 h is when the material is approaching the tertiary creep stage, where microvoids may further interact with dislocations. Such voids nucleation mechanism is also the critical factor that drives long-term creep behaviors in metal welds and heat-affected-zone. For example, Mitsubishi Heavy Industries (MHI) [40] has characterized the microstructures in HAZ during long-term creep for Grade 91 steel and showed that there exists a good correspondence between microvoids density in the HAZ and the overall creep strain acceleration. Voids nucleation model is currently not considered in the present model.

The strain rate dependence upon applied stresses is shown in Fig. 10 (a), where the model prediction agrees very well with the NIMS experimental data. The data point for minimum strain rate ($2.298 \times 10^{-11}\ s^{-1}$) corresponding to the 70 MPa stress at 10,000 h in Fig. 9. Model prediction clearly shows a change in slope at an applied stress of 120 MPa, which is due to the transition to local climb from general climb. The critical applied stress for the onset of local climb mechanism is about 120 MPa, which is consistent with Fig. 5. The apparent stress exponents n_{app} in Fig. 10 (a) are 6.1 and 11.5 for the general climb and local climb regions, respectively, which are above both the typical value for diffusional creep ($n = 1$) and conventional dislocation glide theory ($n = 3$–5) [11]. We emphasize that our calculations do not assume any empirical creep law. The excellent agreement with experimental data indicates that the underlying creep mechanisms have been properly considered.

Table 2
Constant parameter setting.

Parameters	Values	Source
b	0.248 nm	Oruganti [38]
δ	150 nm	Sawada [26]
ν	0.3	Oruganti [38]
θ	2°	Panait [19]
B	8 μm	Panait [19]
S	372 nm	Ennis [21]
K''	70.7 GPa $\sqrt{\text{m}}$	Oruganti [38]
k	0.85	Arzt 1988 [1]

Fig. 10 (b) shows that the model predictions with varying k between 0.75 and 0.85, where the threshold behaviors can be observed. Below the threshold stress, the steady state creep rate contributed by dislocation climb mechanism is negligible. This does not imply that the creep rates are truly zero, but rather indicates that, below these thresholds, other creep mechanisms (e.g., diffusional creep), may become active and must be considered.

From Fig. 10 (b), it is apparent that k values have two distinct effects. First, it effectively modifies the detachment threshold stress, since the athermal stress threshold $\tau_d(0)$ is calculated from Eq. (11) as $\tau_d(0) = \tau_o\sqrt{1-k^2}$. Smaller k value indicates a greater energy reduction at the particle interface, which leads to a stronger threshold behavior with larger threshold stress. For the extreme case of $k = 1$, which indicates the dislocation line energy is unaffected by the particle-matrix interface, the threshold stress due to detachment will vanish since no attractive interaction exits between dislocation line and particles. The second effect of the k value is that it stabilizes the onset of local dislocation segment in Fig. 4.

Returning to the issue of deformation below the threshold stress, the creep model in its current form is based on dislocation-particle interaction mechanisms and cannot be applied to extremely low applied stress case where diffusional creep (e.g., Nabarro-Herring or Coble creep) starts to dominate. Fig. 11 shows the comparison between model prediction and experimental data in a broader range of applied stresses, including the very low stress region where diffusional creep is operating with an apparent stress exponent of unity ($n_{app} = 1$). It is shown that linear extrapolation based on low stress diffusional creep data intersects with NIMS creep data at the applied stress around 50–70 MPa. It also coincides with the detachment threshold stresses, where dislocation climb ceases to be applicable.

4. Conclusions

A dynamic microstructure-sensitive creep modeling framework is developed in order to predict the long-term creep behavior of steel. The model follows Arzt and Rösler's [1] [14], work and assumes the dislocation line energy is reduced at the particle interface as defined in Eq. (5). The dislocation profile during climb process can be calculated based on the condition of minimum energy, which is characterized by a combination between local climb and general climb mode. The line energy reduction introduces a threshold stress when dislocation departs from the particle after the completion of the climb bypass. The threshold stress provides a limit below which the current model ceases to be applicable. Back-stress formulation from Oruganti's work based on the subgrain dislocation structures is integrated into the above dislocation model, as it modifies the applied stress on the dislocations and leads to an effective local stress. The combined model has fully abandoned the empirical assumption of the power-law relationship of steady state creep strain rate, and derives the steady state creep strain rate as a function of creep time and underlying microstructures.

The model prediction of the steady-state creep strain rate for the Grade 91 ferritic steel shows excellent agreement with experimental minimum creep data in the range of applied stress between 50 and 150 MPa as demonstrated in Figs. 10 and 11. As the applied stress increases, a transition of from general climb to local climb is

Table 3
Evolving MX particle parameters as a function of creep time. The values are estimated based on micrographs as reported by Sawada [25].

Time (h)	0	9828	29,827	49,655	70,000
MX radius r (nm)	20.6	20.6	16.3	17.8	15.5
Number density N (/m^2)	8.29×10^{12}	8.58×10^{12}	8.76×10^{12}	5.30×10^{12}	1.34×10^{12}
MX Spacing λ(nm)*	347.5	341.4	338.0	434.3	864.5

*calculated from Eq. (10).

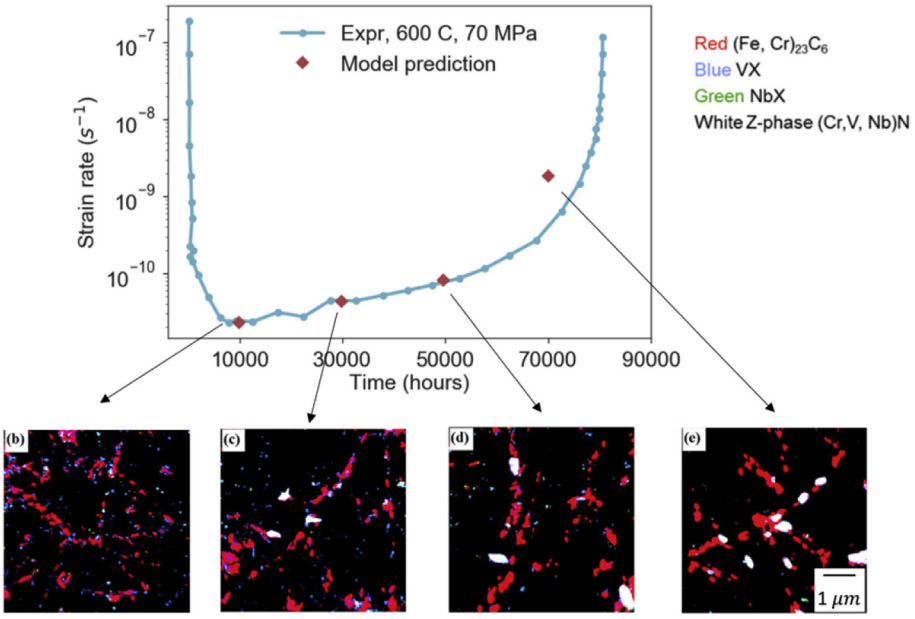

Fig. 8. Comparison between experimental data and model prediction of the strain rate history as a function of time and evolving microstructures of MX particles, for an applied stress of 70 MPa at 600 °C. Microstructure information is obtained from NIMS ([22] [25] [39]).

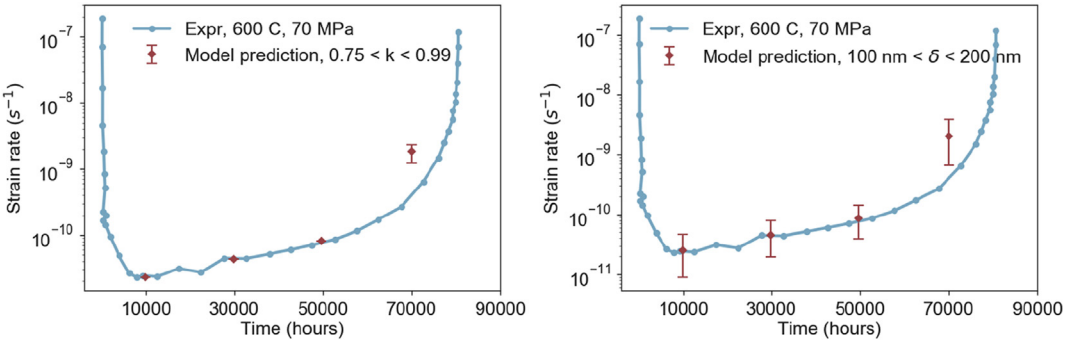

Fig. 9. Parameter sensitivity studies by varying detachment parameter k (left graph) and $M_{23}C_6$ particle spacing δ (right graph). Microstructure information is obtained from NIMS ([22] [25] [39]).

predicted, which results to an increased stress exponent on Fig. 10. The discontinuity of the stress exponent has also been observed by many authors [27] [41], and agrees very well with the model calculation. Necessary model parameters are obtained from microstructure information for the Grade 91 ferritic steel obtained by published literature from NIMS creep database [22] [25], [39]. Not only are the minimum creep rate predicted accurately, but the full creep curve can be predicted (Fig. 10). Also correctly predicted is the threshold stress (Fig. 11), below which dislocation creep is no more active, and diffusional creep (such as Coble and Nabarro creep and grain boundary sliding) control creep deformation; this regime is not modeled here but will be considered in future work. The algorithms developed in this article can further be implemented into finite element method (FEM) analysis, allowing component-level creep analysis of critical steam power plant components. It is noted that the microstructure evolution information during long creep is a critical input of the current model. However, such information which was obtained by interrupted long-term creep test is rarely available in open literature. As an alternative, microstructure modeling software, e.g., thermodynamic software such as *PrecipiCalc*®, can be further utilized to predict the microstructure. These aspects will be pursued as future work.

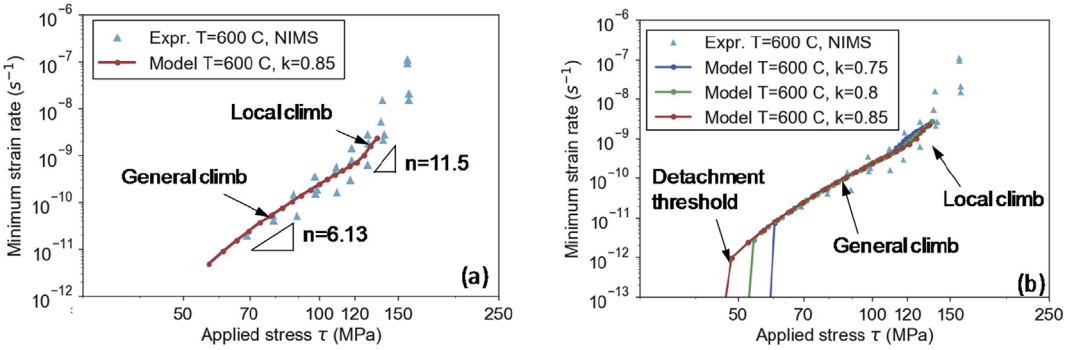

Fig. 10. Minimum strain rate as a function of the applied tensile stress (a) comparison between model prediction between [60 MPa, 130 MPa] and NIMS experimental data ([22] [25], [26] [39]), (b) parameter sensitivity study with different k values in Eq. (5).

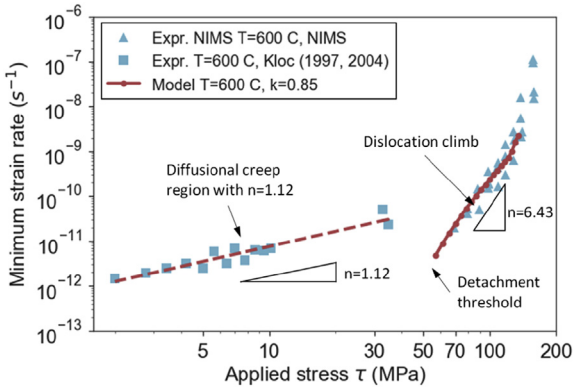

Fig. 11. Comparison between model prediction and experimental data including low applied tensile stress region where diffusional creep is operating with apparent n value n = 1 (data from Kloc and Sklenicka [42] [43]) for Grade 91 steel at 600 C°. The dotted line presents a linear fit of the creep strain rate data with low applied stress. (NIMS creep data is from Refs. [22] [25] [39]).

Acknowledgements

We express our gratitude to the Department of Energy, which supported this research under grant DE-SC0015922.

References

[1] E. Arzt, J. Rosler, The kinetics of dislocation climb over hard particles .2. Effects of an attractive particle dislocation interaction, Acta Metall. 36 (4) (1988) 1053–1060.
[2] Augusto Di Gianfrancesco, Materials for Ultra-supercritical and Advanced Ultra-supercritical Power Plants, 2016.
[3] V. Sklenička, K. Kuchařová, M. Svoboda, L. Kloc, J. Buršík, A. Kroupa, Long-term creep behavior of 9-12%Cr power plant steels, Mater. Char. 51 (1) (2003) 35–48.
[4] J. Hald, High-alloyed martensitic steel grades for boilers in ultra-supercritical power plants, in: Materials for Ultra-supercritical and Advanced Ultra-supercritical Power Plants, 2016, pp. 77–97.
[5] Y. Gorash, Development of a Creep-damage Model for Non-isothermal Long-term Strength Analysis of High-temperature Components Operating in a Wide Stress Range, Martin Luther Univ. Halle-Winttenberg, Halle Ger., 2008.
[6] Romanosky, Introduction and Opening Remarks, in: 26th Annual Conference on Fossil Energy Material, 2012, in: https://www.netl.doe.gov/events/conference-proceedings/2010/fem.
[7] B. Wilshire, P.J. Scharning, A new methodology for analysis of creep and creep fracture data for 9–12% chromium steels, Int. Mater. Rev. 53 (2) (2008) 91–104.
[8] B. Wilshire, P.J. Scharning, Creep ductilities of 9-12% chromium steels, Scripta Mater. 56 (12) (2007) 1023–1026.
[9] B. Wilshire, P.J. Scharning, Long-term creep life prediction for a high chromium steel, Scripta Mater. 56 (8) (2007) 701–704.
[10] B. Wilshire, P.J. Scharning, R. Hurst, A new approach to creep data assessment, Mater. Sci. Eng. 510–511 (C) (2009) 3–6.
[11] M.F. Ashby, H.J. Frost, Deformation-mechanism Maps, Oxford Pergamon Press, 1982, pp. 44–45.
[12] N.M. Ghoniem, G. Po, S. Sharafat, Deformation mechanisms in ferritic/martensitic steels and the impact on mechanical design, J. Nucl. Mater. 441 (1–3) (2013) 704–712.
[13] F.R.N. Nabarro, H.L. Villiers, The physics of creep, Elsevier Sci. 17 (1) (1995) 413.
[14] J. Roesler, E. Arzt, Kinetics of dislocation climb over hard particles - I. climb without attractive particle-dislocation interaction, Acta Metall. 36 (4) (1988) 1043–1051.
[15] R. Lagneborg, Bypassing of dislocations past particles by a climb mechanism, Scripta Metall. 7 (6) (1973) 605–613.
[16] V.C. Nardone, D.E. Matejczyk, J.K. Tien, The threshold stress and departure side pinning of dislocations by dispersoids, Acta Metall. 32 (9) (1984) 1509–1517.
[17] E.A. Marquis, D.C. Dunand, Model for creep threshold stress in precipitation-strengthened alloys with coherent particles, Scripta Mater. 47 (8) (2002) 503–508.
[18] M.E. Krug, D.C. Dunand, Modeling the creep threshold stress due to climb of a dislocation in the stress field of a misfitting precipitate, Acta Mater. 59 (13) (2011) 5125–5134.
[19] C.G. Panait, W. Bendick, A. Fuchsmann, A.F. Gourgues-Lorenzon, J. Besson, Study of the microstructure of the Grade 91 steel after more than 100,000 h of creep exposure at 600°C, Int. J. Pres. Ves. Pip. 87 (6) (2010) 326–335.
[20] M. Tamura, F. Abe, Changes in estimated dislocation density during creep in martensitic heat-resistant steel, J. Mater. Sci. Res. 4 (4) (2015) 48–69.
[21] P.J. Ennis, a. Zielinska-Lipiec, O. Wachter, a. Czyrska-Filemonowicz, Microstructural stability and creep rupture strength of the martensitic steel P92 for advanced power plant, Acta Mater. 45 (12) (1997) 4901–4907.
[22] K. Kimura, K. Sawada, H. Kushima, Y. Toda, Influence of chemical composition and heat treatment on long-term creep strength of grade 91 steel, Procedia Eng. 55 (2013) 2–9.
[23] H. Mughrabi, T. Ungár, W. Kienle, M. Wilkens, Long-range internal stresses and asymmetric X-ray line-broadening in tensile-deformed [001]-orientated copper single crystals, Philos. Mag. A 53 (6) (1986) 793–813.
[24] M.E. Kassner, M.T. Pérez-Prado, K.S. Vecchio, M.A. Wall, Determination of internal stresses in cyclically deformed copper single crystals using convergent-beam electron diffraction and dislocation dipole separation measurements, Acta Mater. 48 (17) (2000) 4247–4254.
[25] K. Sawada, H. Kushima, M. Tabuchi, K. Kimura, Microstructural degradation of Gr.91 steel during creep under low stress, Mater. Sci. Eng. 528 (16–17) (2011) 5511–5518.
[26] K. Sawada, H. Kushima, T. Hara, M. Tabuchi, K. Kimura, Heat-to-heat variation of creep strength and long-term stability of microstructure in Grade 91 steels, Mater. Sci. Eng. 597 (2014) 164–170.
[27] K. Kimura, K. Sawada, H. Kushima, Y. Toda, Region splitting analysis on creep strength enhanced ferritic steels, in: 2007 ASME Press. Vessel. Pip. Conf. - 8th Int. Conf. Creep Fatigue Elev. Temp. PVP-2007/CREEP8, Vol. San Antoni, 2008, pp. 647–654.
[28] R. Kaibyshev, Microstructural evolution in 9%Cr heat resistant steels under creep conditions, Mater. Sci. Forum 715–716 (2012) 813–818.
[29] J.W. Morris, C. Kinney, K. Pytlewski, Y. Adachi, Microstructure and cleavage in lath martensitic steels, Sci. Technol. Adv. Mater. 14 (1) (2013) 14208.
[30] R. Oruganti, M. Karadge, S. Swaminathan, A comprehensive creep model for advanced 9-10% Cr ferritic steels, Procedia Eng. 55 (2013) 727–734.
[31] J. Rösler, E. Arzt, A new model-based creep equation for dispersion strengthened materials, Acta Metall. Mater. 38 (4) (1990) 671–683.
[32] J. Weertman, Theory of steady-state creep based on dislocation climb, J. Appl. Phys. 26 (10) (1955) 1213–1217.
[33] A.S. Argon, S. Takeuchi, Internal stresses in power-law creep, Acta Metall. 29 (11) (1981) 1877–1884.
[34] H. Magnusson, Creep Modelling of Particle Strengthened Steels, 2010.
[35] A.A. Bazazi, Evolution of Microstructure during Long-term Creep of a Tempered Martensite Ferritic Steel, Cuvillier, 2009.
[36] S. Takeuchi, A.S. Argon, Steady-state creep of single-phase crystalline matter

at high temperature, J. Mater. Sci. 11 (8) (1976) 1542–1566.
[37] H. Mughrabi, A two-parameter description of heterogeneous dislocation distributions in deformed metal crystals, Mater. Sci. Eng. 85 (C) (1987) 15–31.
[38] R. Oruganti, M. Karadge, S. Swaminathan, Damage mechanics-based creep model for 9-10%Cr ferritic steels, Acta Mater. 59 (5) (2011) 2145–2155.
[39] K. Sawada, H. Kushima, M. Tabuchi, K. Kimura, Effect of creep deformation on Z phase formation in Gr.91 steel, Mater. Sci. Technol. 30 (1) (2014) 12–16.
[40] N. Komai, T. Tokiyoshi, T. Igari, H. Ohyama, F. Masuyama, K. Kimura, Experimental observation of creep damage evolution in seam-welded elbows of mod. 9Cr-1Mo steel, Mater. A. T. High. Temp. 33 (6) (2016) 617–625.
[41] K. Kimura, K. Sawada, H. Kushima, Y. Toda, Stress dependence of degradation and creep rupture life of creep strength enhanced ferritic steels, in: 5th International Conference on Advances in Materials Technology for Fossil Power Plants vol. Marco Isla, 2008, pp. 601–615.
[42] L. Kloc, V. Sklenička, Transition from power-law to viscous creep behaviour of p-91 type heat-resistant steel, Mater. Sci. Eng. 234–236 (1997) 962–965.
[43] L. Kloc, V. Sklenička, Confirmation of low stress creep regime in 9% chromium steel by stress change creep experiments, Mater. Sci. Eng. 387–389 (1–2 SPEC. ISS) (2004) 633–638.